ADVANCED FUNCTIONAL MATERIALS
www.afm-journal.de

Giant Critical Thickness in Highly Conducting Epitaxial $SrMoO_3$ Electrodes Investigated by Lift-Off Membranes

Yating Ruan, Philipp Schreyer, Tianshu Jiang, Fei Liang, Alexey Arzumanov, Michael Dürrschnabel, Leopoldo Molina-Luna, Philipp Komissinskiy, and Lambert Alff**

Within the huge perovskite materials family, thin films of highly conducting materials such as $SrMoO_3$, $SrNbO_3$, and $SrVO_3$ are candidates for low-loss bottom electrodes in epitaxial all-oxide devices, in particular for high-frequency applications. Recently, the fully coherent growth of more than 5 µm thick $SrMoO_3$ electrodes in a varactor device prototype epitaxial heterostructure has been reported. This result raises the question of the strain mechanism in such anomalously thick coherent epitaxial layers. Here, this question is addressed by comparing the lattice constants of coherently strained layers and their free-standing membranes. $SrMoO_3$ is mainly elastically strained within the heterostructure and fully relaxed after removal of the substrate. These results indicate a giant critical thickness, making highly conducting perovskites even more outstanding materials for high-frequency applications that require electrode thicknesses beyond the skin depth. The described technology of lifting off thick $SrMoO_3$ membranes joins the emerging field of freestanding oxide layer technology, opening unexplored avenues for single crystal investigations, novel perovskite nanostructures, and wafer transfer of functional oxides, walking in the footsteps of recent developments in van der Waals epitaxial heterostructures.

1. Introduction

The low resistivity of 5.1 µΩ cm of $SrMoO_3$ at room temperature, outperforming, for example, Pt, makes this material a promising candidate as an electrode material in epitaxial functional oxide heterostructures for various device applications.[1,2] The high electric conductivity of $SrMoO_3$ originates from both the large electron density beyond 10^{22} cm^{-3} due to two conduction electrons in the 4*d* band of Mo at the *B*-site, and the increased mobility due to reduced electron–electron scattering because of the energetic separation of the *s*- and *d*- bands.[3] Besides their high electric conductivity, $SrMoO_3$ and the related $SrBO_3$ perovskite compounds with (intermixed) Mo, V, and Nb at the *B*-site show intrinsically high optical transparency across and beyond the visible spectral region, making them in addition promising transparent conducting materials.[4–6]

The reported resistivity values of epitaxial $SrMoO_3$ thin films grown by pulsed laser deposition (PLD) and molecular beam epitaxy are well below 50 µΩ cm at room temperature[7–10] with the lowest value even below 20 µΩ cm.[11] Recently, the layer-by-layer growth of 5 µm-thick fully strained epitaxial $SrMoO_3$ films on $GdScO_3$ substrates was reported using PLD, which is well above reported values of critical thicknesses of perovskite epitaxial thin films of similar lattice mismatch.[2] From the viewpoint of electronic device applications, these results revived the concept of all-oxide tuneable capacitors (varactors) in metal-insulator-metal (MIM) geometry.[2,12–16] For making use of all-oxide varactors in microwave circuits, such as phase shifters or tuneable filters for microwave broadband antennas in 5G microelectronic devices, the bottom electrode of the varactor should be thicker than the electromagnetic skin depth in the desired frequency range to minimize electromagnetic losses.[17] For example, $SrMoO_3$ bottom electrodes with a resistivity below 20 µΩ cm and a thickness of more than 5 µm are highly relevant for MIM-type varactors operating at 5 GHz and beyond.

In our previous work, Salg et al. observed cation off-stoichiometry in the $SrMoO_3$ films, specifically an excess of Sr cations.[2] It is well known that the cation off-stoichiometry of epitaxial perovskites is associated with increased lattice constants.[18] Due to the seemingly unrealistic large critical thickness of more than 5 µm, Salg et al. suggested cation self-composed off-stoichiometry as a novel strain accommodation mechanism.[2] The idea was that the material tries to minimize strain energy by incorporating more Sr than Mo during growth. The increase

Y. Ruan, P. Schreyer, T. Jiang, F. Liang, A. Arzumanov, L. Molina-Luna, P. Komissinskiy, L. Alff
Institute of Materials Science
Technische Universität Darmstadt
Peter-Grünberg-Straße 2, 64287 Darmstadt, Germany
E-mail: yating.ruan@tu-darmstadt.de; lambert.alff@tu-darmstadt.de
M. Dürrschnabel
Institute for Applied Materials - Applied Materials Physics
Karlsruhe Institute of Technology
Hermann-von-Helmholtz-Platz 1, 76344 Eggenstein-Leopoldshafen, Germany

The ORCID identification number(s) for the author(s) of this article can be found under https://doi.org/10.1002/adfm.202312508

DOI: 10.1002/adfm.202312508

Table 1. Lattice parameters of the $SrMoO_3$ films and the perovskite scandate substrates used in this work. The lattice parameters of the substrates are given in a pseudocubic notation. The misfit and strain values were calculated relative to the lattice parameters of the relaxed (freestanding) $SrMoO_3$ films. The expected values of the out-of-plane (*c*-axis) lattice parameters of the $SrMoO_3$films, calculated using a Poisson's ratio of 0.271,[31] are given for comparison.

Substrate	Substrate		$SrMoO_3$ (strained)	$SrMoO_3$ (freestanding)		$SrMoO_3$ (Poisson's ratio)	Misfit	Strain	Sr:Mo cation ratio
	a [Å^{-1}]	c [Å^{-1}]	c [Å^{-1}]	a [Å^{-1}]	c [Å^{-1}]	c [Å^{-1}]	[Å]	[%]	
$SmScO_3$	3.989	3.988	3.980	3.984	3.984	3.980	0.005	0.12	1.271
$GdScO_3$	3.968	3.967	3.990	3.983	3.980	3.990	-0.015	-0.38	1.226
$TbScO_3$	3.964	3.951	3.998	3.981	3.981	3.994	-0.017	-0.43	1.202
$DyScO_3$	3.950	3.940	4.003	3.980	3.980	4.002	-0.030	-0.76	1.177

in lattice constant associated with this off-stoichiometry reduces the overall strain energy. To verify this hypothesis, scandates with different rare-earth elements at the *A* site provide an ideal set of substrates to investigate the effect of epitaxial strain on the growth of $SrMoO_3$ thick films.[19] A comparison of the lattice constants in as-grown thin films and their freestanding membranes unambiguously allows to disentangle the origins of strain (relaxation) mechanisms such as elastic strain and effects from self-composed off-stoichiometry.

2. Experimental

In this work, 600 nm-thick $SrMoO_3$ thin films were grown on the (110)-oriented $XScO_3$(X = Dy, Tb, Gd, and Sm) substrates with a size of 5 × 5 mm^2 using pulsed laser deposition (PLD) with a Compex 205 KrF excimer laser by Coherent at a wavelength of 248nm. Before deposition, the PLD chamber was evacuated to a base pressure below 1 × 10^{-8} Torr, and the substrate was heated to a growth temperature of 630 to 700 °C. Then, a 4 nm-thick $SrTiO_3$ buffer layer was grown in vacuum with a laser repetition rate of 2 Hz and a laser fluence of 0.6 J cm^{-2} to ensure layer-by-layer $SrMoO_3$ growth. At the next step, a 600 nm-thick $SrMoO_3$ film was grown with a laser repetition rate of 20 Hz and a laser fluence of 1.0 J cm^{-2} in Ar atmosphere at a pressure of 30 mbar. Film growth was monitored in situ, using a 50 kV reflection high-energy electron diffraction (RHEED) system by Staib Instruments.

With respect to the lift-off procedure, the method developed by Lu et al.,[20] using the water-soluble $Sr_3Al_2O_6$ sacrificial layer, has become one of the most promising techniques for the fabrication of freestanding functional perovskite thin films,[21] such as $SrTiO_3$,[22–24] $SrRuO_3$,[25] $La_{0.7}Sr_{0.3}MnO_3$,[26] $YBa_2Cu_3O_{7-x}$,[27] $BaTiO_3$,[28] and $BiFeO_3$,[24,29] with a range of thicknesses from 50 nm down to a few monolayers.[24] $Sr_3Al_2O_6$ forms a cubic unit cell (space group $Pa\bar{3}$) with a lattice parameter of 15.844 Å, closely matching four unit cells of the stoichiometric $SrMoO_3$ (a = 3.974 Å),[30] as well as the used $XScO_3$ (X = Dy, Tb, Gd, and Sm) substrates (**Table 1**). A $Sr_3Al_2O_6$ sublayer with a thickness of 20 nm was grown in vacuum with a laser fluence of 1.0 J cm^{-2} onto the substrate covered with a $SrTiO_3$ buffer layer. As a next step, additional layers were sequentially deposited, including another $SrTiO_3$ buffer layer, a 600 nm-thick $SrMoO_3$ film, and a top protective $SrTiO_3$ capping layer, forming a heterostructure of $SrTiO_3/SrMoO_3/SrTiO_3/Sr_3Al_2O_6/SrTiO_3/XScO_3$. The $SrTiO_3$ capping layer serves to prevent surface oxidation of the $SrMoO_3$ film during lift-off.[14,15] The thickness of each of the grown $SrTiO_3$ layers was ten unit cells.

A freestanding thin-film heterostructure was obtained as follows: First, a polydimethylsiloxane (PDMS) sheet was attached to the top surface of the as-grown sample. Then the sample was immersed in de-ionized water for ≈1 h to etch away the sacrificial $Sr_3Al_2O_6$ layer and lift the thin-film heterostructure off the scandate substrate. Here, the PDMS sheet served as a mechanical support to stabilize the lifted thin-film heterostructure during its transfer onto another substrate (e.g., Si). Finally, the PDMS sheet was neatly peeled off.

The crystal structure of the films was characterized by X-ray diffraction (XRD), using a SmartLab diffractometer by Rigaku with monochromatic Cu Kα_1 radiation. The lattice parameters of the $SrMoO_3$ films were extracted from the recorded XRD reciprocal space maps (RSM). The values of the out-of-plane lattice parameters obtained from the RSMs correspond with an accuracy of ±0.001 Å to those calculated from the measured XRD 2θ–θ patterns using the Nelson–Riley function. The analysis of the Sr:Mo cation ratio in the $SrMoO_3$ films was carried out by X-ray photoelectron spectroscopy (XPS) with monochromatic Al Kα radiation at elevation angle of 75°, using a PHI Versaprobe 5000 spectrometer. The correlation between the lattice parameters of the $SrMoO_3$ films and their Sr:Mo ratio was additionally studied by density functional theory via the CASTEP package.[32] The exchange-correlation functionals were described within the generalized gradient density approximation (GGA) by Perdew–Burke–Ernzerhof functionals[33] and the ion-electron interactions for all elements were modeled by ultra-soft pseudopotentials.[34] In all calculations, the kinetic energy cut-off of 660 eV and Monkhorst–Pack *k*-point meshes[35] (5 × 5 × 5) were selected to ensure sufficient accuracy of the simulated results. The virtual crystal approximation (VCA)[36] was utilized at the Mo site by a mixed Sr/Mo virtual atom.

3. Results and Discussion

For the first film series, $SrMoO_3/SrTiO_3/XScO_3$ epitaxial thin-film heterostructures were grown to investigate the Sr:Mo cation ratio and lattice parameters of the strained $SrMoO_3$ films. The XRD 2θ–θ patterns of the $SrMoO_3$ films in this series exhibit pronounced 00l reflexes as expected for *c*-axis oriented $SrMoO_3$ (**Figure 1a**). Laue oscillations are observed for the films on $GdScO_3$ substrates, indicating their high crystal quality (inset

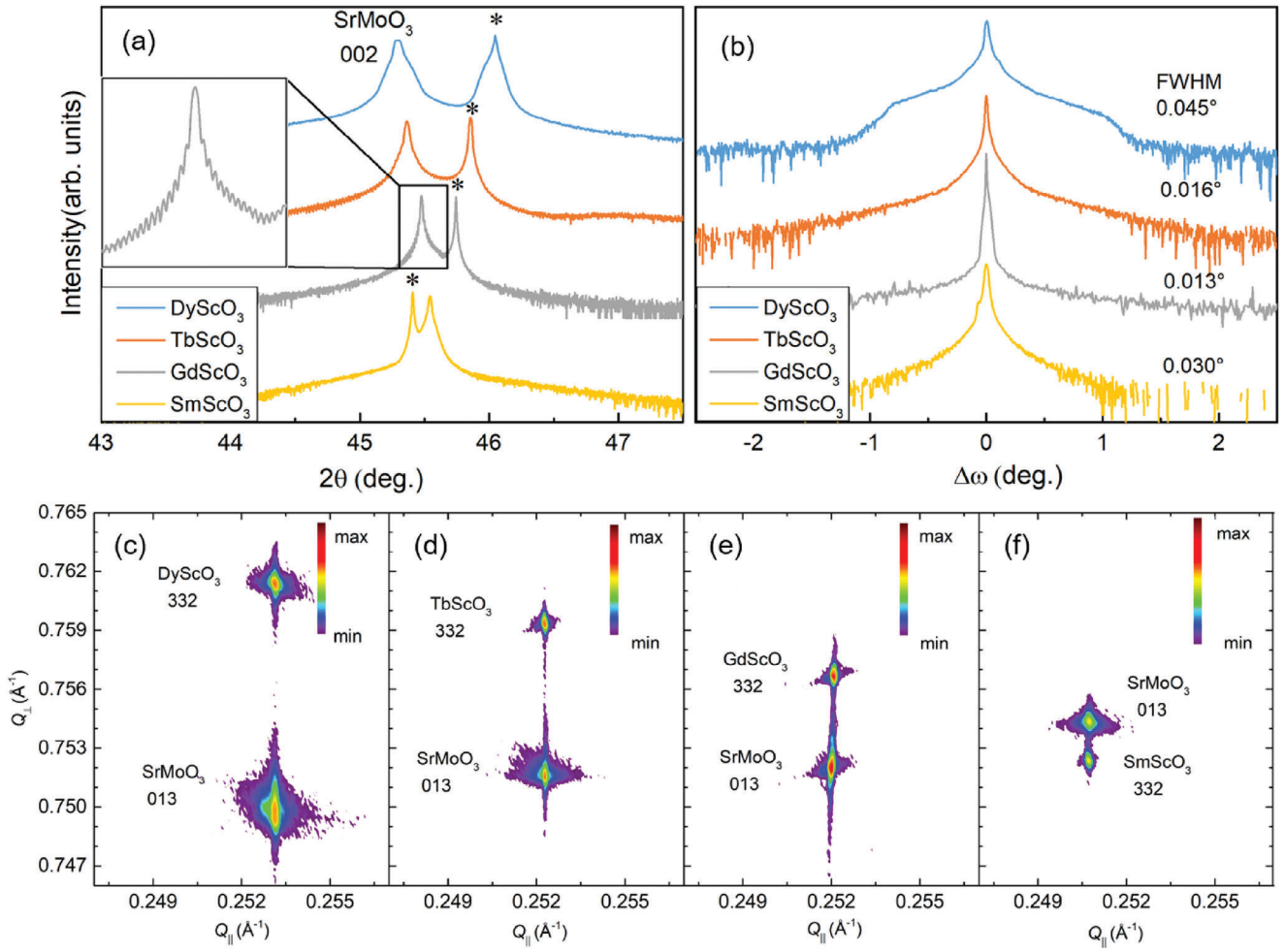

Figure 1. X-ray diffraction of a) 2θ–θ and b) ω scan of the $SrMoO_3$ on the four scandate substrates near the 002 reflections. Stars denote the 220 reflection of scandate substrates. The magnification shows the Laue oscillations of the $SrMoO_3$ film grown on a $GdScO_3$ substrate. c–f) Reciprocal space maps (RSM) near the $XScO_3$ (X = Dy, Gd, Tb, and Sm) 332 reflection of the heterostructures, showing that $SrMoO_3$ films grow in-plane strained on the four substrates.

in Figure 1a). The small period of the Laue oscillations corresponds to the expected 600 nm film thickness. The rocking curves of the $SrMoO_3$ 002 reflex for the films on $GdScO_3$ and $TbScO_3$ substrates exhibit small values of full width at half maximum (FWHM) of 0.013° and 0.016°, respectively, indicating low mosaicity and high crystal quality of the films (Figure 1b). The films on $SmScO_3$ and $DyScO_3$ exhibited increased mosaicity, as evidenced by their rocking curves with FWHM values of 0.03° and 0.45°, respectively. For the $SrMoO_3$ film on $DyScO_3$, the rocking curve shows a wide asymmetric background, which indicates diffusive scattering of X-rays at defects and dislocations. The RSMs of the films of the series (Figure 1c–f) show that the $SrMoO_3$ 013 reflexes are fully aligned in-plane with the 332 substrate reflexes. Thus, the in-plane lattice parameters of the $SrMoO_3$ films fully match the lattice parameters of the substrates. The Sr:Mo ratios of the grown $SrMoO_3$ films (obtained from the XPS studies) are listed in Table 1, showing that the $SrMoO_3$ films are off-stoichiometric with excess Sr. The XPS spectra are available in Supporting Information.

For the second film series, the aim was to fabricate freestanding $SrMoO_3$ films and to investigate the strain relaxation mechanism. The films were grown on $XScO_3$ substrates to form epitaxial thin-film heterostructures of $SrTiO_3/SrMoO_3/SrTiO_3/Sr_3Al_2O_6/SrTiO_3/XScO_3$. The period of the Laue oscillations observed in the 2θ–θ XRD patterns of the as-grown heterostructures on $SmScO_3$ substrate (before lift-off) corresponds to the $Sr_3Al_2O_6$ thickness of 20 nm (**Figure 2a–d**). In general, the crystal quality of the $SrMoO_3$ films in the second series is slightly degraded due to the presence of the $Sr_3Al_2O_6$ sublayer. No dense Laue oscillations from the 600 nm-thick $SrMoO_3$ could be observed. Moreover, the FWHM = 0.11° of the rocking curve of the 002 reflex of the $SrMoO_3$ film on $SmScO_3$ in the second series is larger than that of 0.03° for a similar film in the first series (Figure 2e). However, despite their slightly inferior crystal quality, the $SrMoO_3$ films in the second series grow fully strained on the scandate substrates, as indicated by the vertical alignment in the RSM plot of the 013 film reflexes with the 332 and 0 4 12 reflexes of the substrate and

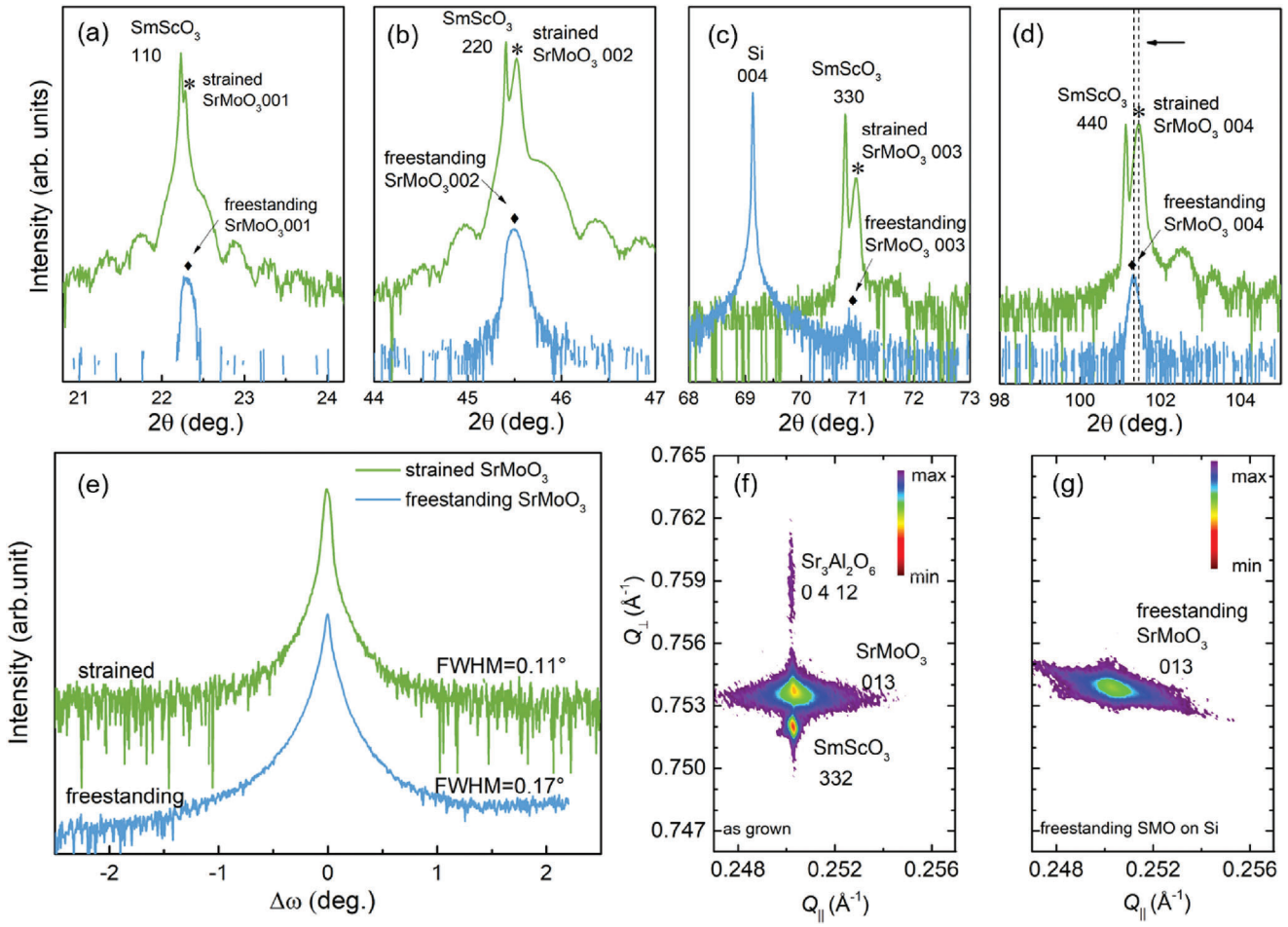

Figure 2. a–d) 2θ–θ X-ray diffraction patterns of the $SrMoO_3$ film strained on the $SmScO_3$ substrate (green) and the freestanding $SrMoO_3$ film (blue) transferred to a Si substrate. The positions of the 00*l* $SrMoO_3$ reflections for the strained and freestanding films are denoted by asterisks and rhombuses, respectively. The 004 Si substrate reflection is shown in (c). e) XRD ω-scan of the (00*l*) reflection of the strained (green) and freestanding (blue) $SrMoO_3$ films, respectively. The reciprocal space maps (RSMs) for the f) strained and g) freestanding $SrMoO_3$ films.

$Sr_3Al_2O_6$ sublayer, respectively (see Figure 2f for the RSM of the $SrMoO_3$ film on $SmScO_3$).

After the lift-off of the heterostructure, the $Sr_3Al_2O_6$ is dissolved in water, and no Laue oscillations could be observed in the 2θ–θ XRD patterns of the freestanding $SrMoO_3$ films (shown in blue in Figure 2a–d). The positions of the 00*l* reflexes of the freestanding $SrMoO_3$ films are slightly shifted relative to those of the epitaxially strained films in the first and second series. The shift is associated with the modified $SrMoO_3$ out-of-plane lattice parameter and increases with the order of the reflex (i.e., with *l*). The largest shift is observed for the 004 $SrMoO_3$ reflex, as denoted by the vertical dashed lines in Figure 2d. A minor degradation in the crystal structure of the freestanding film, as compared with the strained one, is indicated by a practically unchanged shape of the rocking curve of the freestanding $SrMoO_3$ film, with a slight increase of the FWHM to 0.17° (Figure 2e). However, the lattice parameters of the $SrMoO_3$ films change after lift-off, as indicated by the RSM of the freestanding $SrMoO_3$ film on the $SmScO_3$ substrate in Figure 2g.

Figure 3 shows an optical image of a freestanding 1.35 × 2.60 mm^2 $SrMoO_3$ flake that was lifted off the $SmScO_3$ substrate and transferred to a silicon substrate. Parallel cracks in [100] and a few perpendicular cracks in [010] directions are observed. The results of the XRD measurements conducted on two $SrMoO_3$ flakes (transferred to different substrates) indicate that the lattice parameters of freestanding $SrMoO_3$ are stable and independent of the substrate used for the transfer (see Supporting Information).

The lattice parameters of the strained (as-grown) $SrMoO_3$ films of the second series and relaxed (freestanding) $SrMoO_3$ flakes, determined from the XRD measurements, are listed in Table 1. For the strained $SrMoO_3$ films, the in-plane pseudocubic lattice parameter *a* is equal to the lattice parameter of the corresponding substrate. The out-of-plane lattice parameter *c* differs from the in-plane one, thus implying a tetragonal crystal structure of the strained $SrMoO_3$ films. The obtained nearly equal values of the *a* and *c* lattice parameters in the range between 3.980 and 3.984 Å indicate a relaxation of the tetragonal crystal structure to a cubic one for all freestanding $SrMoO_3$ films, lifted off from different scandate substrates. The lattice parameters of the relaxed freestanding $SrMoO_3$ flakes are different from the bulk stoichiometric $SrMoO_3$ lattice parameters (3.974 Å), and thus are considered as the actual bulk lattice parameters of the relaxed cubic

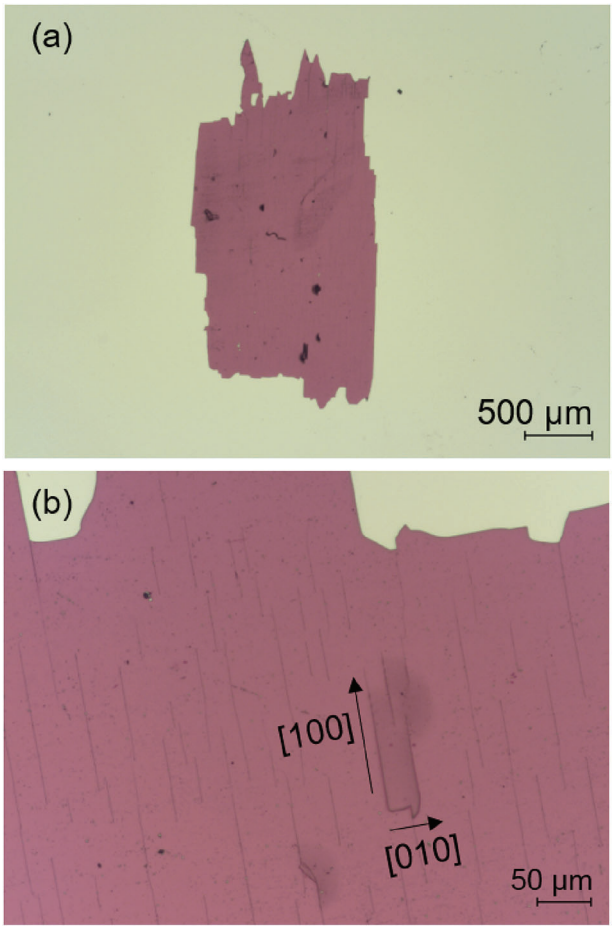

Figure 3. Optical images of a flake of a freestanding $SrMoO_3$ film lifted off a $SmScO_3$ substrate and transferred to a Si substrate. The black arrows show cracks formed along the [100] and [010] crystallographic axes of $SrMoO_3$ during lift-off.

thin film. These actual bulk lattice parameters were used to calculate the misfit and strain values for the strained films presented in Table 1. The smallest absolute value of 0.12% of the biaxial (tensile) strain is realized for the $SrMoO_3$ film on $SmScO_3$ substrate (Table 1). For the other $SrMoO_3$ films on $GdScO_3$, $TbScO_3$, and $DyScO_3$ substrates, the compressive strain is calculated as −0.38%, −0.43%, and −0.76%, respectively. The values of the c lattice parameters of the strained films calculated using the actual bulk lattice parameters of the freestanding films and a $SrMoO_3$ Poisson's ratio ν of 0.271[31] are in very good agreement with the experimental values (Table 1).

Using the actual bulk lattice parameters of the freestanding $SrMoO_3$ films and their strain values, the equilibrium critical thickness (h_c) of $SrMoO_3$ grown on $GdScO_3$ was calculated by the mechanical balance equation described by Matthews and Blakeslee:[37]

$$h_c = \frac{b}{2\pi f}\frac{1-\nu\cos^2\alpha}{(1+\nu)\cos\lambda}\left(\ln\frac{h_c}{b}+1\right) \quad (1)$$

where b is the Burgers vector of the misfit dislocation, f is the misfit strain, α is the angle between the Burgers vector and the dislocation line, and λ is the angle between the slip direction and that direction in the film plane, which is perpendicular to the line of intersection of the slip plane and the interface.[37] The slip system $\{101\}\langle 10\bar{1}\rangle$ is typically realized for a cubic perovskite structure.[38,39] For this slip system, a critical thickness of 74 nm is calculated with Equation (1) for $SrMoO_3$ on $GdScO_3$ using $\cos\alpha = \frac{1}{\sqrt{2}}$, $\cos\lambda = \frac{1}{\sqrt{2}}$, $\nu = 0.271$,[31] $f = 0.0038$, $b = \frac{a_f}{\sqrt{2}}$. Building on Matthews and Blakeslee's framework (Equation (1)), extensive developments and refinements have been made in critical thickness calculations. The kinetics of strain relaxation were taken into account,[40,41] including the rates of dislocation nucleation, propagation, and interaction,[42,43] as well as the stability of dislocation motions[44,45] and the effect of annealing processes.[46] However, using these different modifications to calculate the theoretical critical thickness cannot explain the difference of at least one order of magnitude. While we have considered 600 nm-thick $SrMoO_3$ films in this study, we have previously grown 5 μm-thick $SrMoO_3$ films on $GdScO_3$ substrates without reaching the critical thickness.[2] It is reported for other perovskite oxide thin film systems that the experimentally determined critical thickness can be larger than the theoretically predicted critical thickness, such as MBE-grown 50 nm thick $SrTiO_3$ on $DyScO_3$(110),[39] 50 nm thick $LaCrO_3$ on $SrTiO_3$(001),[47] and 180 nm thick $SrTiO_3$ on LSAT(001).[48] These films relax to a cubic structure with the lattice parameters close to the corresponding bulk values when grown beyond the critical thickness. However, the here studied $SrMoO_3$ films remain strained for their entire thickness and relax only after lift-off in the freestanding state. This observation fundamentally challenges the applicability of the classical mechanical balance approach of critical thickness to $SrMoO_3$.

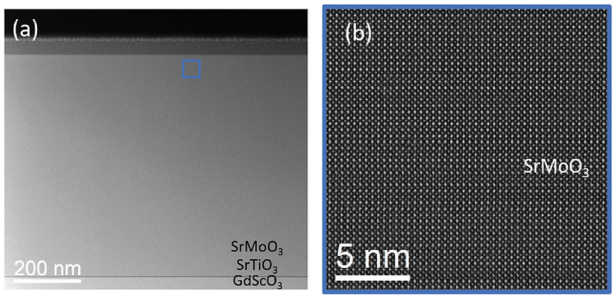

Figure 4. a) HAADF-STEM image of a $SrMoO_3/SrTiO_3/GdScO_3$ heterostructure, showing a long-range homogeneous $SrMoO_3$ film at low magnification. The $SrMoO_3$ in the top region is marked in a blue square. b) Atomic-resolution HAADF-STEM image of $SrMoO_3$ at the region at a thickness of around 600 nm, marked by a blue square and shown in (a).

Supporting these findings, **Figure 4a** shows a low-resolution HAADF-STEM image of the as-grown $SrMoO_3/SrTiO_3/GdScO_3$ heterostructure, and Figure 4b shows a high-resolution image of $SrMoO_3$ close to the surface region (marked by a blue square in Figure 4a). A homogeneous $SrMoO_3$ film is observed in both images without large-scale defects, Sr-excess layers, or strain-induced Ruddlesden–Popper phases, which are typically observed due to strain relaxation of perovskite thin films.[49] No other phases were detected in the XRD measurements of the films in our present and previous work.[2] All these results suggest that the classical mechanical balance approach is unable to explain the giant critical thickness in $SrMoO_3$-thick films.

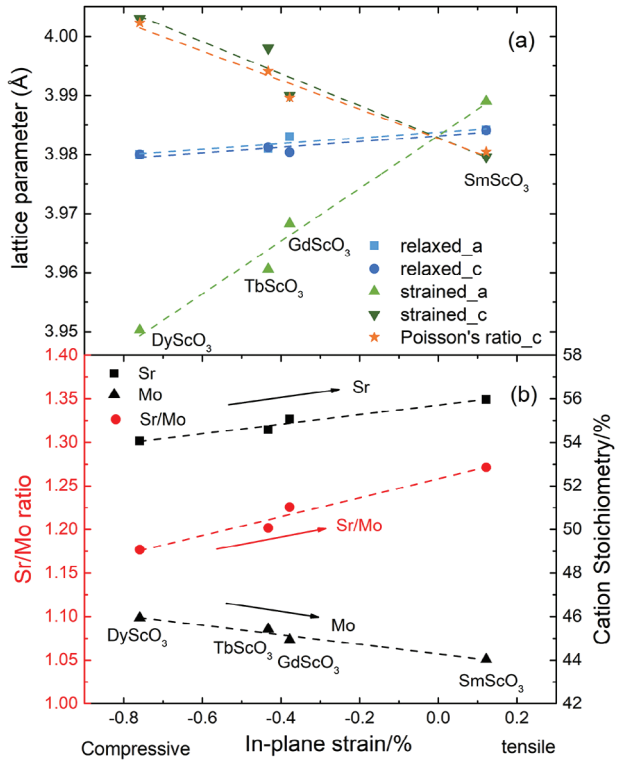

Figure 5. a) Lattice parameters and b) Sr:Mo cation ratio in the $SrMoO_3$ films as a function of epitaxial strain. The dashed straight lines are a guide for an eye.

Although the freestanding $SrMoO_3$ flakes have nearly equal lattice parameters, by closer examination, a subtle yet discernible trend in strain-varied stoichiometry emerges, wherein a slight increasing Sr excess is observed, resulting in a small expansion of lattice parameters in the $SrMoO_3$ films (**Figure 5**). It is noteworthy that this slight change in off-stoichiometry is attributed to strain variations, as the other parameters that are known to cause systematic stoichiometry variations, such as laser fluence, pressure, and substrate temperature, remained constant. The same PLD condition was applied to all samples on different substrates. A homogeneous distribution of cation (Sr and Mo) stoichiometry along the 600 nm thickness of $SrMoO_3$ thin film grown on $SmScO_3$ was observed by TEM-EDX elemental mapping (Supporting Information). Lattice parameters of the $SrMoO_3$ films and the Sr:Mo cation ratio, extracted from the XPS results, are shown in Figure 5 as functions of the actual in-plane strain. The lattice parameter of the freestanding relaxed cubic $SrMoO_3$ films increases slightly linearly with the in-plane strain (Figure 5a). A similar trend is observed for the Sr:Mo cation ratio, namely the increase of Sr excess with the level of in-plane strain from −0.8% to 0.12% (Figure 5a). The results of the DFT calculations show a similar trend (gray triangles in **Figure 6**). Note that the values of the $SrMoO_3$ bulk lattice parameter extracted from the DFT calculations are larger than the obtained corresponding experimental values due to an intrinsic error of GGA-PBE functionals. The (bulk) lattice parameters of 3.980 to 3.984 Å of the films are different from 3.974 Å of the stoichiometric $SrMoO_3$. An extrapolation of this linear dependence to a stoichiometric

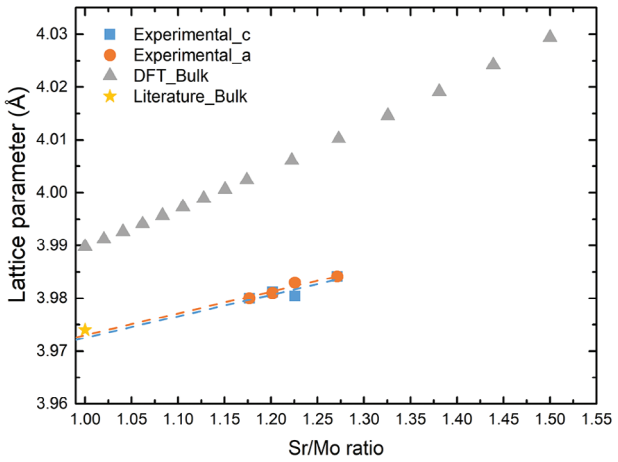

Figure 6. Lattice parameter in $SrMoO_3$ as a function of the Sr/Mo cation ratio. The data are shown for the freestanding $SrMoO_3$ films produced in this work (blue squares and orange circles), stoichiometric $SrMoO_3$ single crystal (yellow star), and for the bulk $SrMoO_3$ with various cation ratios simulated using DFT.

$SrMoO_3$ (Sr:Mo ratio of 1) yields a lattice parameter of 3.973 Å, which nearly perfectly matches the experimental value of 3.974 Å for stoichiometric $SrMoO_3$ single crystals.[1] Thus, the observed trend in off-stoichiometry is considered to be reliable and to reflect the differences between the samples.

4. Conclusion

In summary, 600 nm-thick epitaxial $SrMoO_3$ films were deposited using pulsed laser deposition (PLD) on various perovskite scandate substrates to achieve fully strained films with different levels of epitaxial strains. Remarkably, the thickness of the fully strained epitaxial $SrMoO_3$ films exceeds by far the critical thickness calculated from the classical mechanical balance approach for the given strain value. Through a lift-off process, the films were transferred from the scandate substrates to Si wafers. After the strain relaxation, all the freestanding films exhibited a nearly identical cubic structure. A minor trend of strain-various off-stoichiometry is observed, leading to an expansion of the actual bulk lattice parameters of freestanding $SrMoO_3$ films.

The produced freestanding $SrMoO_3$ films with an area of several square millimeters and a thickness large enough to be regarded as single crystals. Moreover, further increases in their lateral dimensions and thickness are feasible. Combining the unique features of large dimensions, transferability, intrinsic transparency, and high conductivity, $SrMoO_3$ holds great promise for applications in (opto)electronics and energy devices.

Supporting Information

Supporting Information is available from the Wiley Online Library or from the author.

Acknowledgements

This work was funded by the Deutsche Forschungsgemeinschaft (DFG) under Grant No. 206658696, the European Research Council (ERC)

"Horizon 2020" Program under Grant No. 805359-FOXON and Grant No. 957521-STARE.

Open access funding enabled and organized by Projekt DEAL.

Conflict of Interest

The authors declare no conflict of interest.

Data Availability Statement

The data that support the findings of this study are available from the corresponding author upon reasonable request.

Keywords

conducting oxides, epitaxial thin films, giant critical thickness, microelectronics, perovskite

Received: October 11, 2023
Revised: January 10, 2024
Published online:

[1] I. Nagai, N. Shirakawa, S.-i. Ikeda, R. Iwasaki, H. Nishimura, M. Kosaka, *Appl. Phys. Lett.* **2005**, *87*, 024105.
[2] P. Salg, D. Walk, L. Zeinar, A. Radetinac, L. Molina-Luna, A. Zintler, R. Jakoby, H. Maune, P. Komissinskiy, L. Alff, *APL Mater.* **2019**, *7*, 051107.
[3] H. Adachi, *Nat. Phys.* **2015**, *11*, 707.
[4] A. Radetinac, J. Zimmermann, K. Hoyer, H. Zhang, P. Komissinskiy, L. Alff, *J. Appl. Phys.* **2016**, *119*, 055302.
[5] L. Zhang, Y. Zhou, L. Guo, W. Zhao, A. Barnes, H.-T. Zhang, C. Eaton, Y. Zheng, M. Brahlek, H. F. Haneef, N. J. Podraza, M. H. W. Chan, V. Gopalan, K. M. Rabe, R. Engel-Herbert, *Nat. Mater.* **2016**, *15*, 204.
[6] M. Mohammadi, R. Xie, N. Hadaeghi, A. Radetinac, A. Arzumanov, P. Komissinskiy, H. Zhang, L. Alff, *Adv. Mater.* **2023**, *35*, 2206605.
[7] A. Radetinac, K. S. Takahashi, L. Alff, M. Kawasaki, Y. Tokura, *Appl. Phys. Express* **2010**, *3*, 073003.
[8] A. Radetinac, A. Mani, S. Melnyk, M. Nikfalazar, J. Ziegler, Y. Zheng, R. Jakoby, L. Alff, P. Komissinskiy, *Appl. Phys. Lett.* **2014**, *105*, 114108.
[9] J. L. Stoner, P. A. Murgatroyd, M. O'Sullivan, M. S. Dyer, T. D. Manning, J. B. Claridge, M. J. Rosseinsky, J. Alaria, *Adv. Funct. Mater.* **2019**, *29*, 1808609.
[10] H. Takatsu, N. Yamashina, D. Shiga, R. Yukawa, K. Horiba, H. Kumigashira, T. Terashima, H. Kageyama, *J. Cryst. Growth* **2020**, *543*, 125685.
[11] L. Alff, P. Komissinskiy, A. Radetinac, T. Sirman, M. Vafaee, *J. Phys. D. Appl. Phys* **2013**, *47*, 034012.
[12] D. Walk, D. Kienemund, P. Salg, L. Zeinar, A. Radetinac, P. Komissinskiy, L. Alff, R. Jakoby, H. Maune, in *2019 49th European Microwave Conf. (EuMC)*, IEEE, Piscataway, NJ **2019**, pp. 184–187.
[13] D. Walk, P. Salg, D. Kienemund, A. Radetinac, L. Zeinar, C. Schuster, P. Komissinskiy, L. Alff, R. Jakoby, H. Maune, in *2018 48th European Microwave Conf. (EuMC)*, IEEE, Piscataway, NJ **2018**, pp. 563–566.
[14] P. Salg, L. Zeinar, A. Radetinac, D. Walk, H. Maune, R. Jakoby, L. Alff, P. Komissinskiy, *J. Appl. Phys.* **2020**, *127*, 065302.
[15] A. Radetinac, J. Ziegler, M. Vafaee, L. Alff, P. Komissinskiy, *J. Cryst. Growth* **2017**, *463*, 134.
[16] L. Zeinar, P. Salg, D. Walk, S. Petzold, A. Arzumanov, R. Jakoby, H. Maune, L. Alff, P. Komissinskiy, *J. Appl. Phys.* **2020**, *128*, 214104.
[17] S. Gevorgian, *Ferroelectrics in Microwave Devices, Circuits and Systems: Physics, Modeling, Fabrication and Measurements*, 1st ed., Springer, London **2009**.
[18] T. Ohnishi, K. Shibuya, T. Yamamoto, M. Lippmaa, *J. Appl. Phys.* **2008**, *103*, 10.
[19] R. Uecker, B. Velickov, D. Klimm, R. Bertram, M. Bernhagen, M. Rabe, M. Albrecht, R. Fornari, D. Schlom, *J. Cryst. Growth* **2008**, *310*, 2649.
[20] D. Lu, D. J. Baek, S. S. Hong, L. F. Kourkoutis, Y. Hikita, H. Y. Hwang, *Nat. Mater.* **2016**, *15*, 1255.
[21] F. M. Chiabrera, S. Yun, Y. Li, R. T. Dahm, H. Zhang, C. K. Kirchert, D. V. Christensen, F. Trier, T. S. Jespersen, N. Pryds, *Ann. Phys.* **2022**, *534*, 2200084.
[22] Y. Li, C. Xiang, F. M. Chiabrera, S. Yun, H. Zhang, D. J. Kelly, R. T. Dahm, C. K. Kirchert, T. E. L. Cozannet, F. Trier, D. V. Christensen, T. J. Booth, S. B. Simonsen, S. Kadkhodazadeh, T. S. Jespersen, N. Pryds, *Adv. Mater.* **2022**, *34*, 2203187.
[23] R. Xu, J. Huang, E. S. Barnard, S. S. Hong, P. Singh, E. K. Wong, T. Jansen, V. Harbola, J. Xiao, B. Y. Wang, S. Crossley, D. Lu, S. Liu, H. Y. Hwang, *Nat. Commun.* **2020**, *11*, 3141.
[24] D. Ji, S. Cai, T. R. Paudel, H. Sun, C. Zhang, L. Han, Y. Wei, Y. Zang, M. Gu, Y. Zhang, W. Gao, H. Huyan, W. Guo, D. Wu, Z. Gu, E. Y. Tsymbal, P. Wang, Y. Nie, X. Pan, *Nature* **2019**, *570*, 87.
[25] P. T. Le, J. E. Ten Elshof, G. Koster, *Sci. Rep.* **2021**, *11*, 12435.
[26] Z. Lu, J. Liu, J. Feng, X. Zheng, L.-h. Yang, C. Ge, K.-j. Jin, Z. Wang, R.-W. Li, *APL Mater.* **2020**, *8*, 051105.
[27] Z. Chen, B. Y. Wang, B. H. Goodge, D. Lu, S. S. Hong, D. Li, L. F. Kourkoutis, Y. Hikita, H. Y. Hwang, *Phys. Rev. Mater.* **2019**, *3*, 060801.
[28] Q. Wang, H. Fang, D. Wang, J. Wang, N. Zhang, B. He, W. Lü, *Crystals* **2020**, *10*, 733.
[29] Z. Zhao, A. Abdelsamie, R. Guo, S. Shi, J. Zhao, W. Lin, K. Sun, J. Wang, J. Wang, X. Yan, J. Chen, *Nano Res.* **2022**, *15*, 2682.
[30] R. B. Macquart, B. J. Kennedy, M. Avdeev, *J. Solid State Chem.* **2010**, *183*, 250.
[31] N. Kaur, R. Mohan, N. Gaur, R. Singh, *J. Alloys Compd.* **2011**, *509*, 6077.
[32] W. Kohn, *Rev. Mod. Phys.* **1999**, *71*, 1253.
[33] R. Peverati, Y. Zhao, D. G. Truhlar, *J. Phys. Chem.* **2011**, *2*, 1991.
[34] D. Vanderbilt, *Phys. Rev. B* **1990**, *41*, 7892.
[35] J. D. Pack, H. J. Monkhorst, *Phys. Rev. B* **1977**, *16*, 1748.
[36] L. Bellaiche, D. Vanderbilt, *Phys. Rev. B* **2000**, *61*, 7877.
[37] J. Matthews, A. Blakeslee, *J. Cryst. Growth* **1974**, *27*, 118.
[38] J. Speck, W. Pompe, *J. Appl. Phys.* **1994**, *76*, 466.
[39] M. Biegalski, D. Fong, J. Eastman, P. Fuoss, S. Streiffer, T. Heeg, J. Schubert, W. Tian, C. Nelson, X. Pan, M. E. Hawley, M. Bernhagen, P. Reiche, R. Uecker, S. Trolier-McKinstry, D. G. Schlom, *J. Appl. Phys.* **2008**, *104*, 114109.
[40] R. Hull, J. C. Bean, *Crit. Rev. Solid State Mater. Sci.* **1992**, *17*, 507.
[41] S. Jain, A. Harker, R. Cowley, *Philos. Mag. A* **1997**, *75*, 1461.
[42] R. People, J. C. Bean, *Appl. Phys. Lett.* **1985**, *47*, 322.
[43] B. W. Dodson, J. Y. Tsao, *Appl. Phys. Lett.* **1987**, *51*, 1325.
[44] L. Freund, *J. Appl. Mech.* **1987**, *54*, 553.
[45] L. Freund, *MRS Bull.* **1992**, *17*, 52.
[46] R. Hull, J. Bean, C. Buescher, *J. Appl. Phys.* **1989**, *66*, 5837.
[47] L. Qiao, T. C. Droubay, M. E. Bowden, V. Shutthanandan, T. C. Kaspar, S. A. Chambers, *Appl. Phys. Lett.* **2011**, *99*, 6.
[48] T. Wang, K. Ganguly, P. Marshall, P. Xu, B. Jalan, *Appl. Phys. Lett.* **2013**, *103*, 21.
[49] B. Beznosikov, K. Aleksandrov, *Crystallogr. Rep.* **2000**, *45*, 792.